



A novel reduced-basis method with upper and lower bounds for real-time computation of linear elasticity problems

G.R. Liu^{a,b}, Khin Zaw^{a,*}, Y.Y. Wang^c, B. Deng^a

^a Centre for Advanced Computations in Engineering Science, Department of Mechanical Engineering, National University of Singapore, 9 Engineering Drive 1, Singapore 117576, Singapore

^b Singapore-MIT Alliance (SMA), E4-04-10, 4 Engineering Drive 3, Singapore 117576, Singapore

^c Institute of High Performance Computing, Singapore 138632, Singapore

ARTICLE INFO

Article history:

Received 12 February 2008

Received in revised form 22 July 2008

Accepted 23 July 2008

Available online 3 August 2008

Keywords:

Reduced-basis method

Solution bound

Asymptotic error estimation

Linear elasticity

Point interpolation method

Real-time computation

ABSTRACT

This paper presents a novel reduced-basis method for analyzing problems of linear elasticity in a systematic, rapid and reliable fashion for solutions with both upper and lower bounds to the *exact* solution in the form of energy norm or compliance output. The lower bound of the solution output is obtained from the well-known reduced-basis method based on the Galerkin projection used in the finite element method, which is termed as GP_RBM. For the upper bound, a new reduced-basis approach is developed by the combination of the reduced-basis method and a smoothed Galerkin projection used in the linearly conforming point interpolation method, and it is thus termed as SGP_RBM. To examine the present SGP_RBM, we first conduct a theoretical study on the very important upper bound property. Reduced-basis models for both GP_RBM and SGP_RBM are constructed with the aid of an asymptotic error estimation and greedy adaptive procedure. The GP_RBM and the newly proposed SGP_RBM are applied to analyze a cantilever beam with an oblique crack to verify the proposed RBM technique in terms of accuracy, convergence, bound properties and computational savings. Both theoretical analysis and numerical results have demonstrated that the present method is a very efficient method for real-time solutions providing *exact* output bounds.

© 2008 Elsevier B.V. All rights reserved.

1. Introduction

In the design of engineering systems, important quantities (outputs) of interest are usually (i) displacement and stress fields in solids, (ii) flowrates, lift and drag forces in fluids, (iii) temperature and heat flux in thermal systems, etc. These outputs can be computed numerically by solving the PDEs governing the physics of the system. An efficient computational method is thus crucial to solve the PDEs for the desired outputs.

Inventions of the finite element method (FEM) [1–6], the finite difference method (FDM) [6,7], the boundary element method [7] and meshfree methods [8–10] are very important advances in computational methods, and many complicated engineering problems can now be solved routinely. The FEM is the most widely used numerical approach because of the availability of many commercial FEM softwares. A fully compatible FEM model can provide lower bound solutions to the *exact* solution in energy norm or in the form of compliance output for elasticity problems. Meshfree methods have also been developed in recent years. An overview of the meshfree methods and their applications can be found in [8,9].

However, all these numerical methods require a large amount of computing time even for engineering problems of normal-scale. The situation becomes much more critical when one needs to explore intensively in the design space for an optimal design or for inverse analyses of parameter identification [11]. Therefore, reducing computation time is of great importance in the field of numerical simulation for practical engineering applications.

A fast computation method called reduced-basis method [11–13] was proposed with error estimations to solve rapidly engineering systems. Prud'homme et al. [12] introduced the reduced-basis method with a *rigorous* reduced-basis error bound and an asymptotic error bound. The study has shown the efficiency and robustness of reduced-basis method for both compliance and non-compliance outputs. It is observed that the error bound given in these works is actually the error bound for the RBM output with respect to the output of a very fine FEM model. It is not an error bound to the *exact* output of the original problem, because the FEM model surely contains errors. This type of error is thus termed as the reduced-basis approximation error or the RBA-error in this paper for the convenience of presentation. The RBA-error bound is very useful and justified when the FEM model is sufficiently fine and the FEM model error is negligibly small. Nguyen [14] has constructed RBA-error bounds based on an “inf-sup” condition for

* Corresponding author. Tel.: +65 65164797; fax: +65 67791459.
E-mail address: g0402948@nus.edu.sg (K. Zaw).

non-affine and non-linear PDEs. The RBM was also applied to solve inverse problems in his study. In addition, Veroy and Patera [15] presented the reduced-basis method with its rigorous RBA-error bounds for parameterized steady incompressible Navier–Stokes equations. Sen et al. [16] developed “natural norm” of RBA-error estimation for coercive and non-coercive linear elliptic partial differential equations. A stability analysis, for the application of reduced-basis methods to Navier–Stokes equations, based on an “inf–sup” bound condition has been reported by Rozza and Veroy [17]. In addition, applications of the RBM for the Boltzmann equation and stress intensity factor can also be found in [18,19]. All these RBM models use the Galerkin projection and hence are termed as GP_RBM models. Note that the solution bounds in the GP_RBM models are in RBA-errors and very expensive to obtain.

In the recent development in the area of meshfree methods, the linearly conforming point interpolation method (LC-PIM) [20–22] has been formulated using the smoothing operation [23] and PIM [9,10] shape functions. It was found that the LC-PIM has a very important upper bound property in strain energy norm for elasticity problems with homogeneous displacement boundary conditions. This discovery has led to the development of a general procedure to obtain lower and upper bounds to the exact output based on the FEM and the LC-PIM [22] using the same mesh. Based on the idea of the LC-PIM, this paper presents a novel SGP_RBM method that is a reduced-basis method based on the smoothed Galerkin projection. The SGP_RBM permits fast online computation of outputs of interest for linear elasticity problems and provides upper bounds to the exact solution output. The lower bound solution can be produced by the original GP_RBM approach [17]. Therefore, although the exact output for a problem is generally impossible to obtain, we know that it is within the upper and lower bounds using the present fast computation procedure using both GP_RBM and the newly developed SGP_RBM.

This paper is organized as follows. We first brief the important properties of the FEM, the well-known reduced-basis method (RBM), and the LC-PIM method. We next present the formulation for our newly developed SGP_RBM based on the smoothed bilinear form and the smoothed Galerkin projection used in the LC-PIM. We then theoretically prove the upper bound property of our SGP_RBM model. Finally, we implement our SGP_RBM and GP_RBM methods for real-time computation of 2D elasticity problems.

2. Galerkin projection

2.1. Weak formulation

We consider a 2D linear elasticity problem with a physical domain of $\Omega \in \mathbb{R}^2$, and associated functional space of

$$\mathbb{S} = \{ v \in (H^1(\Omega))^2 \mid v_i = 0 \text{ on } \Gamma_D \}, \tag{1}$$

where $H^1(\Omega)$ is a Hilbert space, $v \in \mathbb{S}$ is a trial function, and Γ_D is the boundary on which Dirichlet boundary condition is satisfied. We then introduce the weakform of linear elasticity problem

$$\underbrace{\int_{\Omega} \frac{\partial v_i}{\partial x_j} \left(C_{ijkl} \frac{\partial u_k}{\partial x_l} \right) d\Omega}_{a(u,v)} = \underbrace{\int_{\Gamma_N} v_i t_i d\Gamma + \int_{\Omega} b_i v_i d\Omega}_{f(v)} \tag{2}$$

where $u_i (i = 1, 2)$ is the displacement component in the x_i -directions at a point in Ω , C_{ijkl} is elasticity tensor of material stiffness constants that are symmetrical: $C_{ijkl} = C_{jikl} = C_{ijlk} = C_{klij}$, Γ_N is the boundary on which Neumann boundary condition is satisfied, t_i are the specified boundary stress and b_i are external body force.

The exact solution of the displacement $u^e \in \mathbb{S}$ satisfies

$$a(u^e, v) = f(v) \quad \forall v \in \mathbb{S}. \tag{3}$$

We now define the parameter domain, $\mathcal{D} \in \mathbb{R}^p$. A parameter $\mu \in \mathcal{D}$ is generally an “input” to the problem which may represent the geometry, material properties and/or variety of boundary conditions. Our design problem is now defined as: for a given parameter $\mu \in \mathcal{D}$, the exact output of a given problem can be found by

$$s^e(\mu) = \ell(u^e(\mu); \mu), \tag{4}$$

where ℓ is a μ -parameterized linear functional, and $u^e(\mu) \in \mathbb{S}$ is the exact solution which satisfies

$$a(u^e(\mu), v; \mu) = f(v; \mu) \quad \forall v \in \mathbb{S}, \tag{5}$$

where $a(u^e(\mu), v; \mu)$ and $f(v; \mu)$ are the μ -parameterized bilinear and linear functional, respectively. It shows clearly that evaluating an “output” $s^e(\mu)$ for a given “input” $\mu \in \mathcal{D}$ requests solving the underlying equations as given in Eqs. (4) and (5).

We next define parametric affine mapping which separates typical bilinear form of $a(w, v; \mu)$ to parameter-independent parts and parameter-dependent parts:

$$a(w, v; \mu) = \sum_{q=1}^Q \Theta^q(\mu) a^q(w, v), \tag{6}$$

where $1 \leq q \leq Q$, $\Theta^q(\mu)$ is an affine function of $\mu \in \mathcal{D} \subset \mathbb{R}^p$, and $a^q(w, v)$ is μ -independent bilinear form. Similarly, the typical linear functional can also be defined as

$$f(v; \mu) = \sum_{q_f=1}^{Q_f} \Theta^{q_f}(\mu) f^{q_f}(v), \tag{7}$$

where $1 \leq q_f \leq Q_f$, $\Theta^{q_f}(\mu)$ is an affine functional of $\mu \in \mathcal{D} \subset \mathbb{R}^p$, and $f^{q_f}(v)$ is μ -independent linear functional. The parametric affine mapping is crucial for formulating the affine parameter decomposition [12] which is very important and useful in reduced-basis approximation.

2.2. Finite element approximation

In practice, it is generally very difficult to solve the governing equations either in strong or weakform in analytical means for the exact solution. We then often implement a numerical method to obtain an approximate solution. The most popular method is the traditional finite element method where the standard Galerkin projection is chosen to obtain the approximate solution \tilde{u} . It is well known that such a FEM solution is the best (in energy norm) possible solution in discrete finite element space $\tilde{\mathbb{S}}$ [24], and that $\tilde{u} \rightarrow u$ when $\tilde{\mathbb{S}} \rightarrow \mathbb{S}$, meaning that the FE approximate solution will approach to the exact solution when the size of element approaches to zero and the dimension of the FEM model $\aleph \rightarrow \infty$. In practice, it is not possible to use a FEM model with infinite dimension. However, we can use FEM models of very large dimension \aleph , so that the FEM solution is sufficiently close to the exact solution to meet the design purposes.

For $\mu \in \mathcal{D} \subset \mathbb{R}^p$, the finite element solution \tilde{u} satisfies

$$a(\tilde{u}(\mu), v; \mu) = f(v; \mu) \quad \forall v \in \tilde{\mathbb{S}}. \tag{8}$$

For effective discussion, $\tilde{u}(\mu)$ is expressed in terms of the following interpretation:

$$\tilde{u}(\mu) = \sum_{i=1}^{\aleph} \tilde{u}_i(\mu) \varphi_i, \tag{9}$$

where $\tilde{u}_i(\mu)$ is a nodal displacement at node x_i , and $\varphi_i \in \tilde{\mathbb{S}}$ is a nodal basis (or shape) function constructed based on elements which has delta function property: $\varphi_i(x_j) = \delta_{ij}$.

We then substitute Eq. (9) into Eq. (8), and set $\varphi_i, i = 1, \dots, \aleph$, as the trial function v , we have the following discrete set of \aleph equations.

$$\sum_{j=1}^{\aleph} a(\varphi_j, \varphi_i; \mu) \tilde{u}_j(\mu) = f(\varphi_i; \mu), \quad i = 1, \dots, \aleph \quad (10)$$

or in matrix form

$$\tilde{\mathbf{K}}(\mu) \tilde{\mathbf{u}}(\mu) = \tilde{\mathbf{F}}(\mu). \quad (11)$$

Here, $\tilde{\mathbf{K}}$ is the FEM stiffness matrix with entries of

$$\tilde{K}_{ij}(\mu) = a(\varphi_j, \varphi_i; \mu) = \sum_{q=1}^Q \Theta^q(\mu) a^q(\varphi_j, \varphi_i) \quad (12)$$

or

$$\tilde{\mathbf{K}}(\mu) = \sum_{q=1}^Q \Theta^q(\mu) \tilde{\mathbf{K}}^q, \quad (13)$$

where $\tilde{K}_{ij}^q = a^q(\varphi_j, \varphi_i)$, $1 \leq i, j \leq \aleph$, $\tilde{\mathbf{u}}(\mu)$ is the vector of nodal displacements $\tilde{u}_i(\mu)$, and

$$\tilde{\mathbf{F}}(\mu) = \sum_{q_f=1}^{Q_f} \Theta^{q_f}(\mu) \tilde{\mathbf{F}}^{q_f}, \quad (14)$$

is the vector with entries of

$$\tilde{F}_i(\mu) = f(\varphi_i; \mu) = \sum_{q_f=1}^{Q_f} \Theta^{q_f}(\mu) f^{q_f}(\varphi_i). \quad (15)$$

The corresponding output is defined by

$$\tilde{s} = \ell(\tilde{\mathbf{u}}(\mu)) \quad \text{or} \quad \tilde{s} = \tilde{\mathbf{u}}^T(\mu) \tilde{\mathbf{L}}(\mu), \quad (16)$$

where $\ell = f$ in functional form or $\tilde{\mathbf{L}} = \tilde{\mathbf{F}}$ in matrix form as the compliance output is considered in our work.

The useful and important properties of FEM [4,5,22,25] are briefly as follows.

Remark 2.1. Lower Bound Property: The strain energy based on the compatible FEM solution is no-larger than the exact strain energy.

$$a(\tilde{\mathbf{u}}, \tilde{\mathbf{u}}) = \int_{\Omega} \tilde{\boldsymbol{\varepsilon}}^T \mathbf{C} \tilde{\boldsymbol{\varepsilon}} d\Omega \leq a(\mathbf{u}^e, \mathbf{u}^e) = \int_{\Omega} \boldsymbol{\varepsilon}^T \mathbf{C} \boldsymbol{\varepsilon} d\Omega. \quad (17)$$

In the above equation, the strain energy of the FEM system can also be expressed as

$$a(\tilde{\mathbf{u}}, \tilde{\mathbf{u}}) = \tilde{\mathbf{u}}^T \tilde{\mathbf{K}} \tilde{\mathbf{u}}, \quad (18)$$

and $\tilde{\boldsymbol{\varepsilon}} = \frac{\partial \tilde{\mathbf{u}}}{\partial \mathbf{x}}$ is the strains term related to the FEM displacement $\tilde{\mathbf{u}} \in \tilde{\mathbb{S}} \subset \mathbb{S}$, $\boldsymbol{\varepsilon} = \frac{\partial \mathbf{u}^e}{\partial \mathbf{x}}$ is the exact strain with respect to the exact displacements $\mathbf{u}^e \in \mathbb{S}$. The lower bound property implies the well-known fact that the FEM solution underestimates the strain energy due to the over-stiff behavior of the FEM model.

Remark 2.2. Monotonic property: For given a sequence of n_m nested finite element discretizations D_1, D_2, \dots, D_{n_m} of the corresponding solution space satisfies $\tilde{\mathbb{S}}_{D_1} \subset \tilde{\mathbb{S}}_{D_2} \dots \subset \tilde{\mathbb{S}}_{D_{n_m}} \subset \mathbb{S}$, and the strain energy inequalities then stand

$$a(\tilde{\mathbf{u}}, \tilde{\mathbf{u}})_{D_1} \leq a(\tilde{\mathbf{u}}, \tilde{\mathbf{u}})_{D_2} \leq \dots \leq a(\tilde{\mathbf{u}}, \tilde{\mathbf{u}})_{D_{n_m}} \leq a(\mathbf{u}^e, \mathbf{u}^e), \quad (19)$$

where $a(\tilde{\mathbf{u}}, \tilde{\mathbf{u}})_{D_i}$ is the FEM compatible strain energy obtained using mesh D_i , $1 \leq i \leq n_m$. This property can be shown easily using the arguments give by Oliveira [2].

Remark 2.3. Reproducibility of FEM: If $\mathbf{u}^e \in \tilde{\mathbb{S}}$, then the FEM will reproduce the exact solution. Discussion on this property can be found in Liu [1] and Oliveira [2].

3. Reduced-basis method via Galerkin projection

In general, the computation time for an FEM evaluation is very long due to the very large dimension of the solution space \aleph , and

hence it is very expensive. The reduced-basis approximation was thus developed for computational efficiency and drastic cost reduction.

The standard RBM starts with the introduction of a sample set in the parameter space that is usually very small, $P_N = \{\mu^1 \in \mathcal{D}, \dots, \mu^N \in \mathcal{D}\}$, where $\mu \in \mathcal{D} \subset \mathbb{R}^p$. The reduced-basis space is then defined as $\tilde{\mathbb{W}}_N = \text{span}\{\boldsymbol{\zeta}^i \equiv \tilde{\mathbf{u}}(\mu^i), 1 \leq i \leq N\}$, where $\tilde{\mathbf{u}}(\mu^i)$ is obtainable using the FEM for all given μ^i .

The GP_RBM solution $\tilde{\mathbf{u}}_N(\mu)$, for any $\mu \in \mathcal{D}$, satisfies

$$a(\tilde{\mathbf{u}}_N(\mu), v; \mu) = f(v; \mu) \quad \forall v \in \tilde{\mathbb{W}}_N. \quad (20)$$

where $a(\tilde{\mathbf{u}}_N(\mu), v; \mu)$ is the bilinear form with the properties of symmetry and coercivity [13]. The corresponding output interest can be given by

$$\tilde{s}_N(\mu) = \ell(\tilde{\mathbf{u}}_N(\mu)). \quad (21)$$

3.1. Computational procedure

The GP_RBM solution in terms of displacement field can be written in the form of

$$\tilde{\mathbf{u}}_N(\mu) = \sum_{j=1}^N \tilde{u}_R^j(\mu) \boldsymbol{\zeta}^j, \quad (22)$$

where $\boldsymbol{\zeta}^j = \{\zeta_1^j, \zeta_2^j, \dots, \zeta_N^j\}^T$ is the $\aleph \times 1$ vector of all the nodal displacements of the FEM solution obtained for the j th parameter; $\tilde{u}_R^j(\mu)$ is the unknown reduced-basis coefficient representing the rate of contributions of the bases towards the GP_RBM solution, and is obtained by solving the following set of N equations:

$$\sum_{j=1}^N \left\{ \sum_{q=1}^Q \Theta^q(\mu) a^q(\boldsymbol{\zeta}^j, \boldsymbol{\zeta}^i) \right\} \tilde{u}_R^j(\mu) = \sum_{q_f=1}^{Q_f} \Theta^{q_f}(\mu) f^{q_f}(\boldsymbol{\zeta}^i) \quad (23.a)$$

or in more detail

$$\begin{aligned} \sum_{j=1}^N \left\{ \sum_{q=1}^Q \Theta^q(\mu) \left(\sum_{l=1}^{\aleph} \sum_{k=1}^{\aleph} \zeta_l^q a^q(\varphi_l, \varphi_k) \zeta_k^i \right) \right\} \tilde{u}_R^j(\mu) \\ = \sum_{i=1}^N \sum_{q_f=1}^{Q_f} \Theta^{q_f}(\mu) \left(\sum_{k=1}^{\aleph} \zeta_k^i f^{q_f}(\varphi_k) \right) \end{aligned} \quad (23.b)$$

where $i = 1, \dots, N$. Note that both a^q and f^{q_f} are computed offline and very expensive, but need only to be done once. We further provide the equations in matrix form in order to present the reduced-basis procedure in mechanics community, and the matrix forms are very helpful for the proofs in this study.

Eq. (23) can be written in the following matrix form:

$$\tilde{\mathbf{K}}_N(\mu) \tilde{\mathbf{u}}_N(\mu) = \tilde{\mathbf{F}}_N(\mu), \quad (24)$$

where $\tilde{\mathbf{u}}_N(\mu)$ is a reduced-basis coefficient vector with the entries of $\tilde{u}_R^j(\mu)$. Following Eqs. (6) and (7), the reduced-basis stiffness matrix and force vector are defined as

$$\tilde{\mathbf{K}}_N(\mu) = \sum_{q=1}^Q \Theta^q(\mu) \tilde{\mathbf{K}}_N^q \quad \text{and} \quad \tilde{\mathbf{F}}_N(\mu) = \sum_{q_f=1}^{Q_f} \Theta^{q_f}(\mu) \tilde{\mathbf{F}}_N^{q_f}, \quad (25)$$

where $\tilde{\mathbf{K}}_N^q$ is a parameter-independent $N \times N$ matrix and $\tilde{\mathbf{F}}_N^{q_f}$ is a parameter-independent $N \times 1$ vector:

$$\tilde{\mathbf{K}}_N^q = \mathbf{Z}^T \tilde{\mathbf{K}}^q \mathbf{Z} \quad (26)$$

and

$$\tilde{\mathbf{F}}_N^{q_f} = \mathbf{Z}^T \tilde{\mathbf{F}}^{q_f}, \quad (27)$$

where

$$\mathbf{Z} = [\boldsymbol{\zeta}^i \equiv \tilde{\mathbf{u}}(\mu^i), 1 \leq i \leq N] \quad (28)$$

with a dimension of $\aleph \times N$, $\tilde{\mathbf{K}}^q$ is a $\aleph \times \aleph$ matrix with the entries of $a^q(\varphi_j, \varphi_i)$, and $\tilde{\mathbf{F}}^q$ is a $\aleph \times 1$ vector with entries of $f^q(\varphi_i)$. In the GP_RBM formulation, it should be noted that all the bases of $\tilde{\mathbb{W}}_N$ must be linearly independent in order to obtain the well-conditioned RBM algebraic equation. Hence the Gram–Schmidt orthogonalization is employed to orthogonalize the bases of $\tilde{\mathbb{W}}_N$, and thus the matrix \mathbf{Z} is made orthogonal [13].

The discrete form of output defined by Eq. (21) can be written as

$$\tilde{s}_N(\mu) = \tilde{\mathbf{u}}_N(\mu)^T \tilde{\mathbf{L}}_N(\mu) = \tilde{\mathbf{u}}_N(\mu)^T \tilde{\mathbf{F}}_N(\mu), \quad (29)$$

where $\tilde{\mathbf{L}}_N = \tilde{\mathbf{F}}_N$ for our compliance output.

From the above formulation, the procedure of GP_RBM can be separated into “offline” and “online” computational stages [12,13]. In the “offline” stage, N times of finite element analyses based on the mesh of very large dimension \aleph are required to evaluate, and thus very expensive. The matrices \mathbf{Z} , $\tilde{\mathbf{K}}_N^q$ and $\tilde{\mathbf{F}}_N^q$ need to be formed “offline” and stored. In the “online” computational stage, Eq. (25) is necessary to form for an input parameter $\mu \in \mathcal{D} \subset \mathbb{R}^p$. Eqs. (24) and (29) are then solved for the RB output. Therefore, the online computation basically requires $O(N^3)$ operations to obtain the reduced-basis output of interest $\tilde{s}_N(\mu)$ very efficiently and virtually in real-time.

3.2. Properties of the Galerkin projection reduced-basis method

We now provide some important and useful properties of the GP_RBM.

Remark 3.1. Lower bound property: The strain energy of the GP_RBM solution is a lower bound to that of the full FEM solution and also that of the exact solution:

$$a(\tilde{u}_N, \tilde{u}_N) \leq a(\tilde{u}, \tilde{u}) \leq a(u^e, u^e), \quad (30)$$

where $\tilde{u}_N \in \tilde{\mathbb{W}}_N$, $\tilde{u} \in \tilde{\mathbb{S}}$, $u^e \in \mathbb{S}$ and $\tilde{\mathbb{W}}_N \subset \tilde{\mathbb{S}} \subset \mathbb{S}$.

The proof is very simple and straightforward based on the symmetry and coercivity of $a(\cdot, \cdot)$. As the GP_RBM uses the standard Galerkin projection that is the same projection that one uses for creating the standard FEM model, it produces a lower bound solution (in energy norm) to the FEM solution and hence to the exact solution (see, Remark 2.1). The proof of this remark can be found in [12,13].

Remark 3.2. Monotonic convergence property: For given a sequence of n_m nested finite element discretizations D_1, D_2, \dots, D_{n_m} , such that the corresponding solution spaces satisfy $\mathbb{S}_{D_1} \subset \mathbb{S}_{D_2} \subset \dots \subset \mathbb{S}_{D_{n_m}} \subset \mathbb{S}$. The reduced-basis spaces based on the given sequence of meshes can also anticipate that $(\tilde{\mathbb{W}}_N)_{D_1} \subset (\tilde{\mathbb{W}}_N)_{D_2} \subset \dots \subset (\tilde{\mathbb{W}}_N)_{D_{n_m}} \subset \tilde{\mathbb{S}}_{D_{n_m}}$, where $(\tilde{\mathbb{W}}_N)_{D_i}$ is the reduced-basis space based on the mesh D_i . From Remark 2.2 and Remark 3.1, we then have the following inequality:

$$a(\tilde{u}_N, \tilde{u}_N)_{D_1} \leq a(\tilde{u}_N, \tilde{u}_N)_{D_2} \leq \dots \leq a(\tilde{u}_N, \tilde{u}_N)_{D_{n_m}} \leq a(u^e, u^e), \quad (31)$$

where $a(\tilde{u}_N, \tilde{u}_N)_{D_i}$ are the strain potential energy of the GP_RBM based on the FEM mesh D_i .

4. Smoothed Galerkin weakform

To establish the theoretical framework of an upper bound reduced-basis method, a smoothed Galerkin weakform is introduced based on a smoothed bilinear form. In the smoothed bilinear form, the gradient of field variables is modified by using the strain smoothing operation [23] which provides a softening effect to the discretized model. The softening effect can lead to an upper bound solution with respect to the FEM solution as well as the exact solution. Therefore, numerical methods developed based on the

smoothed bilinear form are proven variationally consistent and can possess a very important upper bound property. The smoothed Galerkin weakform is very powerful for a new class of numerical methods. Examples of numerical techniques based on the smoothed Galerkin weakform are the stabilization technique for nodal integrated meshfree methods where nodal-based smoothing domains of Voronoi cells are used [23]; the smoothed finite element method (SFEM) where element-based smoothing cells are used [26,27]; the LC-PIM where nodal-based smoothing cells and PIM shape functions are used for upper bound solutions [20,28]; the edge-smoothed finite element method where edge-based smoothing domain and PIM shape functions are used [29].

4.1. Smoothed bilinear form

The problem domain Ω is divided into a set of N_n smoothing domains/cells Ω_n , such that $\Omega = \cup_{n=1}^{N_n} \Omega_n$, as shown in Fig. 1. The integral representation of a function $w \in \mathbb{S}$ is firstly introduced [9] as

$$w^{IR}(\mathbf{x}) = \int_{\Omega_n} w(\xi) \widehat{W}(\mathbf{x} - \xi) d\xi, \quad (32)$$

where the superscript “IR” stands for integral representation, and $\widehat{W} \in \mathbb{S}$ is a pre-described smoothing function for the point at \mathbf{x} in the smoothing domain Ω_n . It is required that (1) function w is at least first order differentiable over the smoothing domain Ω_n and (2) the smoothing function $\widehat{W} \in \mathbb{S}$ should have the properties of positivity, decay and partition of unity: $\int_{\Omega_n} \widehat{W}(\mathbf{x} - \xi) d\xi = 1$, so that at least the constant function at \mathbf{x} can be exactly represented at the limit of $\Omega_n \rightarrow 0$. The simplest smoothing function is the local constant smoothed function is defined as

$$\widehat{W}(\mathbf{x} - \xi) = \overline{W}(\mathbf{x} - \xi) = \begin{cases} 1/A_n & \xi \in \Omega_n, \\ 0 & \xi \notin \Omega_n, \end{cases} \quad (33)$$

where $A_n = \int_{\Omega_n} d\Omega$ is the area of Ω_n in which the point \mathbf{x} is included. Assuming that $w \in \mathbb{S}$ is differentiable and the first derivatives of a function w can be represented as

$$\begin{aligned} \left(\frac{\partial w_i(\mathbf{x})}{\partial x_j} \right)^{IR} &= \int_{\Omega_n} \frac{\partial w_i(\xi)}{\partial x_j} \widehat{W}(\mathbf{x} - \xi) d\xi = \left(\frac{1}{A_n} \int_{\Omega_n} \frac{\partial w_i(\xi)}{\partial x_j} d\xi \right) \\ &\equiv \overline{\frac{\partial w_i}{\partial x_j}}. \end{aligned} \quad (34)$$

Eq. (34) suggests that $\left(\frac{\partial w_i(\mathbf{x})}{\partial x_j} \right)^{IR}$ is now a constant in Ω_n , and then using the well-known Green’s Theorem, the smoothed strain/gradient of Eq. (34) becomes the line-integral form:

$$\overline{\frac{\partial w_i}{\partial x_j}} = \frac{1}{A_n} \int_{\Gamma_n} w_i n_j d\Gamma, \quad (35)$$

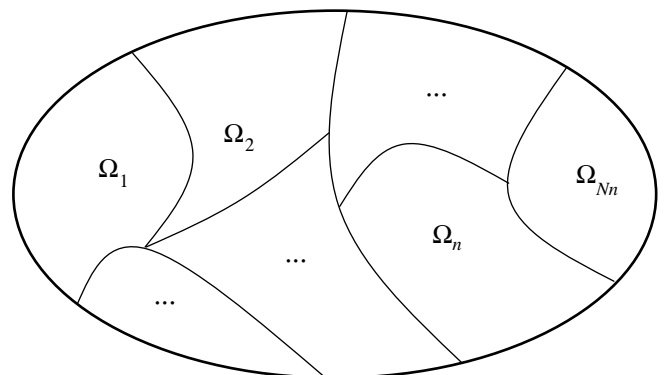


Fig. 1. Division of problem domain Ω into smoothing domains Ω_n .

where Γ_n is the boundary of the smoothing domain Ω_n and n_j is the outward normal on Γ_n . Note that Eq. (35) is also well-known as the distributional derivative of a function in the classical sense, and when w is continuous, Eq. (35) is the exact expression for the smoothed derivative. Liu has generalized Eq. (35) to cases when w is discontinuous living in a G space [25]. In this work, however, we confirm our discussion only in H spaces.

Using the smoothed gradient defined in Eq. (35), the smoothed bilinear form can be written as

$$\begin{aligned} \bar{a}_D(w, v) &= \int_{\Omega} \frac{\partial v_i}{\partial x_j} C_{ijkl} \frac{\partial w_k}{\partial x_l} d\Omega \\ &= \sum_{n=1}^{N_n} \frac{1}{A_n} \left(\int_{\Gamma_n} v_i n_j d\Gamma \right) \left(C_{ijkl} \int_{\Gamma_n} w_k n_l d\Gamma \right). \end{aligned} \quad (36)$$

Here, we assume that C_{ijkl} is constant (not a function of coordinate).

4.2. Linearly conforming point interpolation method

As in the FEM, the LC-PIM physical domain Ω is first meshed with N_e elements of, say, triangles with total of N_n nodes because the triangular mesh can be created automatically for complicated problem domains. In the LC-PIM, these triangular cells/elements are then divided into N_n smoothing domains $\Omega = \cup_{n=1}^{N_n} \Omega_n$, and each Ω_n contains a node and covers portions of elements sharing the node, as shown in Fig. 2. For any $\mu \in \mathcal{D} \subset \mathbb{R}^p$, the LC-PIM seeks the solution that satisfies the smoothed Galerkin weakform:

$$\bar{a}_D(\bar{u}(\mu), v; \mu) = f(v; \mu) \quad \forall v \in \tilde{\mathcal{S}}, \quad (37)$$

where displacement field $\bar{u}(\mu) \in \tilde{\mathcal{S}}$ is expressed in terms of the following interpretation

$$\bar{u}(\mu) = \sum_{i=1}^{\aleph} \bar{u}_i(\mu) \varphi_i, \quad (38)$$

where $\bar{u}_i(\mu)$ is a nodal displacement, and $\varphi_i \in \tilde{\mathcal{S}}$ is a nodal shape function of the point interpolation method. In the point interpolation method (PIM), shape functions are constructed using a set of scattered nodes in a local support domain. The procedure of constructing PIM shape function, based on polynomial functions, is very straightforward and generally the same as the traditional finite element method but using nodes beyond the element. The detailed procedure can be found in [9]. In this work, we use only three nodes in constructing PIM shape functions φ_i which is the same as that of the linear triangular element in the FEM.

We then substitute Eq. (38) into Eq. (37), and set $\varphi_i, i = 1, \dots, \aleph$, as the trial function v , we have the following discrete set of \aleph equations.

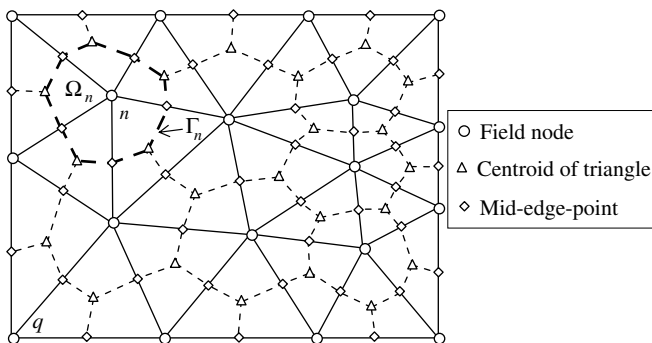


Fig. 2. Illustration of background triangular mesh and the smoothing domain created by sequentially connecting the centroids with the mid-edge-points of the surrounding triangles of a node.

$$\sum_{j=1}^{\aleph} \bar{a}_D(\varphi_j, \varphi_i; \mu) \bar{u}_j(\mu) = f(\varphi_i; \mu), \quad i = 1, \dots, \aleph. \quad (39)$$

In the matrix form, it can also be written as

$$\bar{\mathbf{K}}(\mu) \bar{\mathbf{u}}(\mu) = \bar{\mathbf{F}}(\mu), \quad (40)$$

where $\bar{\mathbf{K}}(\mu)$ is the smoothed stiffness matrix of LC-PIM with entries of $\bar{\mathbf{K}}_{ij}(\mu) = \bar{a}(\varphi_j, \varphi_i; \mu)$, $1 \leq i, j \leq \aleph$, $\bar{\mathbf{u}}(\mu)$ is the vector of nodal displacements $\bar{u}_i(\mu)$, and $\bar{\mathbf{F}}(\mu)$ is the vector with entries of $f(\varphi_i; \mu)$, which is the same as given in the FEM. Similar to the FEM, the LC-PIM of Eq. (40) follows Eqs. (11)–(15).

The corresponding output is defined by

$$\bar{s}(\mu) = \ell(\bar{u}(\mu)) = \bar{\mathbf{u}}^T(\mu) \bar{\mathbf{L}}(\mu), \quad (41)$$

where $\bar{\mathbf{L}} = \bar{\mathbf{F}}$ for our compliance case.

4.3. Properties of the linearly conforming point interpolation method

The properties of our smoothed bilinear form and the LC-PIM are now listed here. The proofs of these properties can be found in [22] based on energy principle, in [25] based on variational statement for functions in H spaces, and in [30] for functions in G spaces.

Remark 4.1. Reproducibility property: When the smoothing domain $\Omega_n \rightarrow 0$, the smoothing function $\bar{W}(\mathbf{x} - \xi)$ becomes the Delta function and the smoothing strain $\frac{\partial \bar{w}_i}{\partial x_j}$ approaches to the exact strain of $\frac{\partial w_i(\mathbf{x})}{\partial x_j}$. Thus, we shall have $\bar{a}_D(w, v) \rightarrow a(w, v)$.

Remark 4.2. The formulation of LC-PIM (see Eq. (36)) clearly indicates that the smoothed bilinear form of LC-PIM is symmetric: $\bar{a}_D(w, v) = \bar{a}_D(v, w), \forall w, v \in \tilde{\mathcal{S}}$ and positive definite: $\bar{a}(w, w) > 0 \forall w \in \mathcal{S}, w \neq 0$.

Remark 4.3. Softening effects: For any $u \in \mathcal{S}$, we have the inequality: $\bar{a}_D(u, u) \leq a(u, u)$, where $\bar{a}_D(\cdot)$ is the smoothed bilinear form given in Eq. (36) and $a(\cdot)$ is the standard bilinear form given in Eq. (2).

Remark 4.4. For any $u \in \tilde{\mathcal{S}}$, the strain energy for a LC-PIM model is no-larger than that of a FEM model: $\bar{a}_D(u, u) \leq a(u, u)$, where $\bar{a}_D(u, u) = \mathbf{u}^T \bar{\mathbf{K}} \mathbf{u}$ and $a(u, u) = \mathbf{u}^T \mathbf{K} \mathbf{u}$.

Remark 4.4 is a general consequence of Remark 4.3. It also indicates that the FEM stiffness matrix \mathbf{K} is “stiffer” than the LC-PIM stiffness matrix $\bar{\mathbf{K}}$.

Remark 4.5. Upper bound of the FEM solution: The strain energy of the smoothed Galerkin projection solution \bar{u} is no-less than that of the FEM solution \tilde{u} : $a(\bar{u}, \bar{u}) \leq \bar{a}_D(\bar{u}, \bar{u})$ where $\bar{a}_D(\bar{u}, \bar{u}) = \bar{\mathbf{u}}^T \bar{\mathbf{K}} \bar{\mathbf{u}}$ and $a(\tilde{u}, \tilde{u}) = \tilde{\mathbf{u}}^T \tilde{\mathbf{K}} \tilde{\mathbf{u}}$ in matrix form.

Remark 4.6. Monotonic convergence property: The LC-PIM possesses the monotonic convergence property. For domain discretizations: D_1 and D_2 , we have the inequality: $\bar{a}_{D_1}(w, w) \leq \bar{a}_{D_2}(w, w)$, where the domain division D_1 is created by dividing the problem domain Ω into a set of smoothing domains: $\Omega = \cup_{n=1}^{N_n} \Omega_n$, and the division D_2 is created by sub-dividing the smoothing domains Ω_n of D_1 into sub-smoothing-domains: $\Omega_n = \cup_{d=1}^{d_s} \Omega_{n,d}$ [25].

Proof. According to the smoothing domain divisions of D_1 and D_2 described above, the contribution of Ω_n and that of sub-smoothing-domains $\Omega_n = \cup_{d=1}^{d_s} \Omega_{n,d}$ should be compared, and thus we should have

$$\int_{\Omega_n} \frac{\partial w_i}{\partial x_j} d\Omega = \sum_{d=1}^{d_s} \int_{\Omega_{n,d}} \frac{\partial w_i}{\partial x_j} d\Omega. \quad (42)$$

Using the above equation and the *triangular inequality* [25], we have the following inequality:

$$\begin{aligned} & \frac{1}{A_n} \left(\int_{\Omega_n} \frac{\partial w_i}{\partial x_j} d\Omega \right) C_{ijkl} \left(\int_{\Omega_n} \frac{\partial w_k}{\partial x_l} d\Omega \right) \\ &= \frac{1}{A_n} \left(\sum_{d=1}^{d_s} \int_{\Omega_{n,r}} \frac{\partial w_i}{\partial x_j} d\Omega \right) C_{ijkl} \left(\sum_{d=1}^{d_s} \int_{\Omega_{n,r}} \frac{\partial w_k}{\partial x_l} d\Omega \right) \\ &\leq \frac{1}{A_n} \sum_{d=1}^{d_s} \left[\left(\int_{\Omega_{n,r}} \frac{\partial w_i}{\partial x_j} d\Omega \right) C_{ijkl} \left(\int_{\Omega_{n,r}} \frac{\partial w_k}{\partial x_l} d\Omega \right) \right]. \end{aligned} \quad (43)$$

Eq. (43) implies Remark 4.6.

In this work, we should note that the creation of smoothing domains Ω_n , in the LC-PIM, is based on the background cells/elements as shown in Fig. 2. When the size of elements to approaching zero, so does the smoothing domains $\Omega_n \rightarrow 0$. From Remark 4.1, it is noted that if $\Omega_n \rightarrow 0$, we have $\bar{a}_D(w, v) \rightarrow a(w, v)$. This shows that the LC-PIM solution will approach to the *exact* solution and the softening effect introduced by the smoothed Galerkin projection is monotonically reduced, when the mesh is refined in a nested manner. \square

Remark 4.7. *Existence of upper bound of the exact solution:* For a fixed division of smoothing domains D , there always exists a sufficiently large critical dimension of the discretized space \aleph_c , such that when $\aleph \geq \aleph_c$, the strain energy of the smoothed Galerkin solution \bar{u} can be uniquely found and is no-less than that of the *exact* solution u^e : $\bar{a}_D(\bar{u}, \bar{u}) \geq a(u^e, u^e)$.

Proof. We first examine

$$\bar{a}_D(\bar{u}, \bar{u}) - a(u^e, u^e) = \underbrace{[\bar{a}_D(\bar{u}, \bar{u}) - a(\bar{u}, \bar{u})]}_{\Delta_{SG-G}} - \underbrace{[a(u^e, u^e) - a(\bar{u}, \bar{u})]}_{\delta_{Ex-G}}, \quad (44)$$

where

$$\delta_{Ex-G} = a(u^e, u^e) - a(\bar{u}, \bar{u}) \geq 0 \quad (45)$$

This is the gap between the *exact* solution and the Galerkin (FEM) solution. From Remark 2.2, we know that δ_{Ex-G} is a non-negative number that approaches to zero when the mesh is refined ($\aleph \rightarrow \infty$). On the other hand, from Remark 4.5, we have

$$\Delta_{SG-G} = \bar{a}_D(\bar{u}, \bar{u}) - a(\bar{u}, \bar{u}) \geq 0. \quad (46)$$

This is the gap between the smoothed Galerkin solution and the Galerkin solution. It is a non-negative *finite* number of a *fixed* finite smoothing domain division D for any given mesh division \aleph . The gap Δ_{SG-G} will never approach to zero regardless how big \aleph is, if a smoothing domain division D is kept finite. This is because Δ_{SG-G} represents the smoothing effects depending only on how the smoothing is operated. It approaches to zero only when the smoothing domain Ω_n is refined. Therefore, Eq. (44) becomes

$$\underbrace{\bar{a}_D(\bar{u}, \bar{u}) - a(u^e, u^e)}_{\geq 0 \text{ when } \aleph \uparrow} = \underbrace{\Delta_{SG-G}}_{\geq 0 \text{ and finite for any } \aleph} - \underbrace{\delta_{Ex-G}}_{\rightarrow 0 \text{ when } \aleph \uparrow} \quad (47)$$

Therefore, there exist always an \aleph that is sufficiently large, so that $\bar{a}_D(\bar{u}, \bar{u}) \geq a(u^e, u^e)$. This proves Remark 4.7. \square

Note Remark 4.7 is just to show the fact that we can always make a smoothed Galerkin model as soft as desired. In fact, when \aleph increase too much in relation to a fixed finite smoothing domain division D , the smoothed Galerkin model can even become singular, and \bar{u} can not be able to obtained. Even in that case, Remark 4.7 can still hold, because \bar{u} becomes infinite and so $\bar{a}_D(\bar{u}, \bar{u})$. In

our past work so far, Remark 4.7 was confirmed using LC-PIM [22]. Discussions on the minimum number of smoothing domains in relations to the number of DOFs (or nodes) for a non-singular smoothed Galerkin model can be found in [25,30].

5. A novel reduced-basis method

The main purpose of this study is to develop a novel RBM approach that produces an upper bound of the *exact* output for linear elasticity solid mechanics problems. The idea is inspired from the formulation of the linear conforming point interpolation method (LC-PIM) [20,21]. The novel RBM model is built by the smoothed Galerkin projection and thus termed as the smoothed Galerkin projection reduced-basis method (SGP_RBM). We now present the computational procedure of SGP_RBM in both variational formulation and matrix formulation.

In the SGP-RBM, the basic procedures are largely the same as that of the GP_RBM presented earlier. The key difference is that we use the smoothed bilinear form in the SGP_RBM. The SGP_RBM starts with a sample set $P_N = \{\mu^1 \in \mathcal{D}, \dots, \mu^N \in \mathcal{D}\}$ that is usually very small, where $\mu \in \mathcal{D} \subset \mathbb{R}^p$, and the reduced-basis space $\bar{\mathbb{W}}_N = \text{span}\{\zeta^i \equiv \bar{u}(\mu^i), 1 \leq i \leq N\}$, as defined in Section 3. The SGP_RBM solution for any $\mu \in \mathcal{D}$ satisfies

$$\bar{a}_D(\bar{u}_N(\mu), v; \mu) = f(v; \mu) \quad \forall v \in \bar{\mathbb{W}}_N, \quad (48)$$

where $\bar{u}_N(\mu)$ is the SGP_RBM solution. Following the GP_RBM computational procedure as discussed in Section 3.1, the above equation (48) can be written as

$$\sum_{j=1}^N \left\{ \sum_{q=1}^Q \Theta^q(\mu) \bar{a}_D^q(\zeta^j, \zeta^i) \right\} \bar{u}_R^j(\mu) = \sum_{q_f=1}^{Q_f} \Theta^{q_f}(\mu) f^{q_f}(\zeta^i), \quad 1 \leq i \leq N, \quad (49.a)$$

$$\begin{aligned} & \sum_{j=1}^N \left\{ \sum_{q=1}^Q \Theta^q(\mu) \left(\sum_{l=1}^N \sum_{k=1}^N \zeta_l^j \bar{a}_D^q(\varphi_l, \varphi_k) \zeta_k^i \right) \right\} \bar{u}_R^j(\mu) \\ &= \sum_{i=1}^N \sum_{q_f=1}^{Q_f} \Theta^{q_f}(\mu) \left(\sum_{k=1}^N \zeta_k^i f^{q_f}(\varphi_k) \right), \end{aligned} \quad (49.b)$$

where $\bar{a}_D^q(\cdot, \cdot)$ is the smoothed bilinear form for component q , and \bar{u}_R^j are the unknown SGP_RBM contribution rates to the bases of $\bar{\mathbb{W}}_N$. The terms \bar{a}_D^q and f^{q_f} are computed offline, but only once.

The matrix form of the discretized system equation can be expressed as

$$\bar{\mathbf{K}}_N(\mu) \bar{\mathbf{u}}_N(\mu) = \bar{\mathbf{F}}_N(\mu). \quad (50)$$

In the above equation, $\bar{\mathbf{u}}_N(\mu)$ is a $N \times 1$ vector with the entries of $\bar{u}_R^j(\mu)$; the stiffness matrix $\bar{\mathbf{K}}_N$ of $N \times N$ is defined as

$$\bar{\mathbf{K}}_N(\mu) = \left(\sum_{q=1}^Q \Theta^q(\mu) \bar{\mathbf{K}}_N^q \right), \quad (51)$$

where $\bar{\mathbf{K}}_N^q = \mathbf{Z}^T \bar{\mathbf{K}}^q \mathbf{Z}$ with the matrix \mathbf{Z} given in Eq. (28), and $\bar{\mathbf{K}}^q$ is a $\aleph \times \aleph$ smoothed stiffness matrix with the entries of $\bar{a}_D^q(\varphi_j, \varphi_i)$. The force term is defined as

$$\bar{\mathbf{F}}_N(\mu) = \sum_{q_f=1}^{Q_f} \Theta^{q_f}(\mu) \bar{\mathbf{F}}_N^{q_f}, \quad (52)$$

where $\bar{\mathbf{F}}_N^{q_f} = \mathbf{Z}^T \bar{\mathbf{F}}^{q_f}$ is the $N \times 1$ reduced-basis force vector and $\bar{\mathbf{F}}^{q_f}$ is the $\aleph \times 1$ force vector containing $f^{q_f}(\varphi_i)$.

The SGP_RBM output can be written as

$$\bar{s}_N(\mu) = \ell(\bar{u}_N(\mu)) = \bar{\mathbf{u}}_N(\mu)^T \bar{\mathbf{L}}_N(\mu). \quad (53)$$

Similar to the GP_RBM, the computational procedure of the SGP_RBM can also be separated into the “offline” and “online” computational stages. The “offline” and “online” computations for both GP_ and SGP_RBM are listed in Table 1 for clear reference.

5.1. Properties of the novel reduced-basis method

Remark 5.1. *Softening effect:* For any admissible $u_N \in \widetilde{\mathbb{W}}_N$, the strain potential energy for the SGP_RBM is no-larger than that for the GP_RBM:

$$\bar{a}_D(u_N, u_N) \leq a(u_N, u_N), \quad (54)$$

where

$$\bar{a}_D(u_N, u_N) = \mathbf{u}_N^T \bar{\mathbf{K}}_N \mathbf{u}_N = \mathbf{u}_N^T (\mathbf{Z}^T \bar{\mathbf{K}} \mathbf{Z}) \mathbf{u}_N \quad (55)$$

and

$$a(u_N, u_N) = \mathbf{u}_N^T \tilde{\mathbf{K}}_N \mathbf{u}_N = \mathbf{u}_N^T (\mathbf{Z}^T \tilde{\mathbf{K}} \mathbf{Z}) \mathbf{u}_N, \quad (56)$$

where $\bar{a}_D(u_N, u_N)$ and $a(u_N, u_N)$ are bilinear forms of the SGP_RBM and the GP_RBM based on any admissible displacement field u_N .

Remark 5.1 is the consequence of Remark 4.4 and can be said loosely that $\bar{\mathbf{K}}_N$ is softer than $\tilde{\mathbf{K}}_N$.

Remark 5.2. *Upper bound to the GP_RBM solution:* The strain energy of the SGP_RBM is an upper bound to that of the GP_RBM: $\bar{a}_D(\bar{u}_N, \bar{u}_N) \geq a(\tilde{u}_N, \tilde{u}_N)$.

Proof. From Eqs. (20) and (48), we can have

$$\bar{a}_D(\bar{u}_N, v) = a(\tilde{u}_N, v), \quad \forall v \in \widetilde{\mathbb{W}}_N. \quad (57)$$

If we define $v = \tilde{u}_N$, we obtain

$$\bar{a}_D(\bar{u}_N, \tilde{u}_N) = a(\tilde{u}_N, \tilde{u}_N). \quad (58)$$

Similarly, if we define $v = \bar{u}_N$, we obtain

$$\bar{a}_D(\bar{u}_N, \bar{u}_N) = a(\tilde{u}_N, \bar{u}_N). \quad (59)$$

We next define the error $\bar{u}_N - \tilde{u}_N$, and examine the following:

$$\begin{aligned} \underbrace{\bar{a}_D(\bar{u}_N - \tilde{u}_N, \bar{u}_N - \tilde{u}_N)}_{\geq 0} &= \bar{a}_D(\bar{u}_N, \bar{u}_N) - 2\bar{a}_D(\bar{u}_N, \tilde{u}_N) + \bar{a}_D(\tilde{u}_N, \tilde{u}_N) \\ &= \bar{a}_D(\bar{u}_N, \bar{u}_N) - 2a(\tilde{u}_N, \bar{u}_N) + \bar{a}_D(\tilde{u}_N, \tilde{u}_N) \\ \underbrace{(a(\tilde{u}_N, \bar{u}_N) - \bar{a}_D(\tilde{u}_N, \tilde{u}_N))}_{\geq 0} + a(\tilde{u}_N, \tilde{u}_N) &\leq \bar{a}_D(\bar{u}_N, \bar{u}_N) \end{aligned} \quad (60)$$

From the argument of Remark 5.1, we have $(a(\tilde{u}_N, \bar{u}_N) - \bar{a}_D(\tilde{u}_N, \tilde{u}_N)) \geq 0$. Therefore, the above equation confirms this Remark 5.2. \square

Remark 5.3. *Monotonic convergence property:* Based on the two domain divisions: D_1 for a coarse mesh and D_2 for a fine mesh, we have the following inequality:

$$\bar{a}_{D_1}(\bar{u}_N, \bar{u}_N) \geq \bar{a}_{D_2}(\bar{u}_N, \bar{u}_N), \quad (61)$$

Table 1
Offline and online evaluations of GP_ and SGP_RBM

| Stage | GP_RBM | SGP_RBM | Dimension |
|--------------------|--|---------------------------|--------------|
| Offline evaluation | \mathbf{Z} (both GP_ and SGP_RBM) | | $N \times N$ |
| | $\bar{\mathbf{F}}^{qf}$ (both GP_ and SGP_RBM) | | $N \times 1$ |
| | $\bar{\mathbf{F}}_N^{qf}$ (both GP_ and SGP_RBM) | | $N \times 1$ |
| | $\bar{\mathbf{K}}_N^{qf}$ | $\bar{\mathbf{K}}_N^{qf}$ | $N \times N$ |
| Online evaluation | $\bar{\mathbf{F}}_N$ (both GP_ and SGP_RBM) | | $N \times 1$ |
| | $\bar{\mathbf{K}}_N$ | $\bar{\mathbf{K}}_N$ | $N \times N$ |
| | $\bar{\mathbf{u}}_N$ | $\bar{\mathbf{u}}_N$ | $N \times 1$ |
| | \bar{s}_N | \bar{s}_N | Scalar value |

where $\bar{a}_{D_i}(\bar{u}_N, \bar{u}_N)$ is the strain potential energy of SGP_RBM based on the mesh D_i .

Remark 5.3 is a consequence of Remark 4.6.

Remark 5.4. *Upper bound of the FEM solution:* For a fixed division of smoothing domain D , there always exists a sufficiently large critical dimension of the reduced-basis space N_c , such that when $N \geq N_c$ the strain potential energy $\bar{a}_D(\bar{u}_N, \bar{u}_N)$ of the SGP_RBM solution is no-less than $a(\tilde{u}, \tilde{u})$ of the FEM solution: $\bar{a}_D(\bar{u}_N, \bar{u}_N) \geq a(\tilde{u}, \tilde{u})$.

Proof. From Remark 3.1, we have

$$\Delta' = a(\tilde{u}, \tilde{u}) - a(\tilde{u}_N, \tilde{u}_N) \geq 0. \quad (62)$$

Here, we note the fact that Δ' is a non-negative number that approaches to zero when the RBM space is refined ($N \rightarrow \infty$). On the other hand, from Remark 5.2, we have

$$\Delta'' = \bar{a}_D(\bar{u}_N, \bar{u}_N) - a(\tilde{u}_N, \tilde{u}_N) \geq 0. \quad (63)$$

Note, now the important fact that Δ'' is a non-negative finite number of a fixed finite smoothing domain division D for any given N . The gap Δ'' will never approach to zero regardless how big the N is, if D is finite. It approaches to zero only when the smoothing domain D is refined. Using Eqs. (62) and (63), we then obtain

$$\bar{a}_D(\bar{u}_N, \bar{u}_N) - a(\tilde{u}, \tilde{u}) = \Delta'' - \Delta'. \quad (64)$$

Now, we can observe a situation: for a fixed D , when $N \rightarrow \infty$, $\tilde{u}_N \rightarrow \tilde{u}$ and $\Delta' \rightarrow 0$ but Δ'' remains non-negative and finite:

$$\underbrace{\bar{a}_D(\bar{u}_N, \bar{u}_N) - a(\tilde{u}, \tilde{u})}_{-\Delta' \text{ when } N \rightarrow \infty} = \underbrace{\Delta''}_{\text{non-negative and finite for any } N} - \underbrace{\Delta'}_{\rightarrow 0 \text{ when } N \rightarrow \infty}. \quad (65)$$

Therefore, we can always find an N that is sufficiently large, so that $\bar{a}_D(\bar{u}_N, \bar{u}_N) \geq a(\tilde{u}, \tilde{u})$. This proves Remark 5.4. \square

Remark 5.5. *Upper bound to the exact solution:* For a fixed division of smoothing domain D , there always exists sufficiently large numbers N_c and N_c^* , such that when $N \geq N_c$ and $N \geq N_c^*$, the strain energy of SGP_RBM solution is no-less than that of the exact solution: $\bar{a}_D(\bar{u}_N, \bar{u}_N) \geq a(u^e, u^e)$, if the smoothing operation is sufficient in the model.

Remark 5.5 is the consequence of Remark 4.7 and Remark 5.4. It will be confirmed later in our numerical study.

5.2. Output bound and the bound gap

We now examine the upper and lower bounds of the present RBM to the exact output. From the properties of GP_RBM and SGP_RBM (Remark 3.1 and Remark 5.5), we have our compliance output bound:

$$\tilde{s}_N(\mu) \leq s^e(\mu) \leq \bar{s}_N(\mu), \quad (66)$$

where

$$\tilde{s}_N = \tilde{\mathbf{u}}_N^T \tilde{\mathbf{F}}_N = \tilde{\mathbf{u}}_N^T \tilde{\mathbf{K}}_N \tilde{\mathbf{u}}_N \equiv a(\tilde{u}_N, \tilde{u}_N) \quad (67)$$

is the lower bound output of the GP_RBM model and similarly,

$$\bar{s}_N = \bar{\mathbf{u}}_N^T \bar{\mathbf{F}}_N = \bar{\mathbf{u}}_N^T \bar{\mathbf{K}}_N \bar{\mathbf{u}}_N \equiv a(\bar{u}_N, \bar{u}_N) \quad (68)$$

is the upper bound output of the SGP_RBM model in the form of energy norm. Since the exact output bounds have been known, we need only a model that is just fine enough for our practical design. The use of unnecessarily fine model that are very expensive can be avoided.

The output bound gap is determined by

$$G_D(\mu) = \bar{s}_N(\mu) - \tilde{s}_N(\mu), \quad (69)$$

where $G_D(\mu)$ is the bound gap, and the subscript “D” stands for discretization. By comparing the bound gaps $G_{D_1}(\mu)$ and $G_{D_2}(\mu)$, it is possible to assert that the use of the fine mesh in the proposed reduced-basis method will have a tighter bound gap than that of the coarse mesh: $G_{D_1}(\mu) \geq G_{D_2}(\mu)$, based on the monotonic convergence property of GP_ and SGP_RBM (Remark 3.2 and Remark 5.3). It is noted that the bound gap $G_D(\mu)$ is employed for verifying monotonic convergence property of the proposed reduced-basis method.

6. Sample set construction

The creation of reduced-basis sample set follows that in reference [11]. The asymptotic error estimation and the greedy adaptive procedure are the ingredients of the sample set construction.

6.1. Asymptotic error estimation

In the reduced-basis method, the “N” optimal sample set P_N and associated “N” RB space \widetilde{W}_N need to be created. Thus, a simple RBA-error estimation using the greedy adaptive procedure is employed to determine optimal “N”. In this work, the asymptotic error estimate [11,12] is chosen as a RBA-error estimation. We first define an alternate “M” sample set in the parameter space, $P_M = \{\mu^1 \in \mathcal{D}, \dots, \mu^M \in \mathcal{D}\}$ and the associated “doubled” reduced-basis space becomes $\widetilde{W}_M = \text{span}\{\tilde{u}(\mu^1), \dots, \tilde{u}(\mu^M)\}$, where $M = 2N$. We intentionally set $P_N \subset P_M$ and consequently $\widetilde{W}_N \subset \widetilde{W}_M$; it is possible to expect that the “M” reduced-basis solution $\tilde{u}_M(\mu)$ is very close to $\tilde{u}(\mu)$, $\tilde{u}_M(\mu) \rightarrow \tilde{u}(\mu)$ and thus $\tilde{s}_M(\mu) \rightarrow \tilde{s}(\mu)$ due to fast convergence rate of the reduced-basis approximation [13]. The “M” RBM solution output can thus be treated as the traditional FEM solution output in the error estimation.

The asymptotic estimate error introduced by GP_ RBM is defined as

$$A_{N,M}^s(\mu) = |\tilde{s}_M(\mu) - \tilde{s}_N(\mu)|, \quad (70)$$

and the exact error is also presented as

$$A_{N,\text{exact}}^s(\mu) = |\tilde{s}(\mu) - \tilde{s}_N(\mu)|, \quad (71)$$

to justify the reliability and accuracy of our asymptotic error estimation. Based on the asymptotic error bound [11–13], the asymptotic error estimation has the desirable features of theoretical simplicity, computational efficiency, a very close-to-unity affectivity, and thus it can be expected that $A_{N,M}^s(\mu) \approx A_{N,\text{exact}}^s(\mu)$. Besides, the asymptotic error estimation works well for many types of outputs. Therefore, it is very suitable for the creation of our reduced-basis sample set.

The averaged asymptotic and exact errors defined below are used to examine the performance of our procedures in a predefined random parameter set $S_{\text{test}} \subset \mathcal{D}$.

$$A_{N,M,\text{avg}}^s = \frac{\sum_{i=1}^{n_{\text{test}}} A_{N,M}^s(\mu_{\text{test}}^i)}{n_{\text{test}}} \quad \text{and} \quad (72)$$

$$A_{N,\text{exact},\text{avg}}^s = \frac{\sum_{i=1}^{n_{\text{test}}} A_{N,\text{exact}}^s(\mu_{\text{test}}^i)}{n_{\text{test}}},$$

where $\mu_{\text{test}}^i \in S_{\text{test}}$, $A_{N,M}^s(\mu_{\text{test}}^i)$ and $A_{N,\text{exact}}^s(\mu_{\text{test}}^i)$ are evaluated using Eqs. (70) and (71), respectively.

6.2. Greedy adaptive procedure

In the greedy algorithm, a sample space S^G is necessarily created in a regular grid pattern over the entire parameter domain \mathcal{D} . Sampling points $\mu^i \in P_N$ are chosen in $S^G \subset \mathcal{D}$ to create an optimal reduced-basis sample set $P_N = \{\mu^i; 1 \leq i \leq N\}$ here. At the i th greedy step, a sample point $\mu^i \in P_N$ is chosen at which the maximum

asymptotic error point $A_{N,M}^s(\mu_{\text{max}}^i)$ is found. At a certain “N” greedy step, it is found that the maximum asymptotic error $A_{N,M}^s(\mu_{\text{max}}^N) \leq \varepsilon_{\text{tol}}$, where ε_{tol} is the predefined output error tolerance, and the greedy algorithm will stop. The optimal sample set construction is completed.

Note that creating reduced-basis sample set P_N is only based on the GP_RBM model as (i) the bases of RB spaces: \widetilde{W}_N and \widetilde{W}_M are spanned by the FEM approximations, (ii) the exact error $A_{N,\text{exact}}^s(\mu)$ is based on the FEM solution, and (iii) both GP_ and SGP_RBM models use the same P_N (and \widetilde{W}_N) conveniently. The use of the same \widetilde{W}_N results in saving a certain computational cost for our SGP_RBM model as no extra RB space is necessary to create for our SGP_RBM.

7. Numerical example and results

We now present a numerical example of a two-dimensional cantilever beam with an oblique crack to examine the GP_RBM and SGP_RBM in terms of (i) numerical convergency, (ii) output-bound properties and (iii) computational efficiency.

7.1. Problem definition

Consider a two-dimensional linear elasticity problem of an isotropic cantilever beam of physical domain $\Omega \in \mathbb{R}^2$. The beam containing an oblique crack in the middle plane is characterized by the three parameters: the crack length denoted by L , the inclined angle θ and the position of the crack center b , as shown in Fig. 3. We can thus define the “input” parameter $\mu \equiv (b, L, \theta) \in \mathcal{D} = [1.5, 2.5] \times [0.3, 0.7] \times [15^\circ, 75^\circ] \subset \mathbb{R}^3$. We assume that the material properties of the beam are of unit density, unity Young modulus and Poisson ratio of $\nu = 0.25$. The plane stress problem is considered. The boundary condition is then defined: the Dirichlet boundary conditions on the boundary Γ_D , pressure or normal traction on Γ_T and zero traction on the surface of the crack Γ_C , the right edge Γ_R and the bottom surface Γ_B . The output of our problem is a compliance output which is the average displacement along the upper boundary of the beam, Γ_T .

In this work, the FEM mesh consisting of linear triangular elements with a total degree of freedom of $\mathfrak{N} = 17,344$ as shown in Fig. 4 is first used for both GP_ and SGP_RBM. The GP_RBM and SGP_RBM are coded to analyze this problem for real-time solution. The numerical results are presented in the following section.

7.2. Numerical results

7.2.1. Convergence

To choose an optimal reduced-basis sample set P_N , a regular sampling grid of $17 \times 17 \times 17$ for parameters $\mu \equiv (b, L, \theta)$ of $S^G \subset \mathcal{D}$ is used in the greedy adaptive procedure. The desired accu-

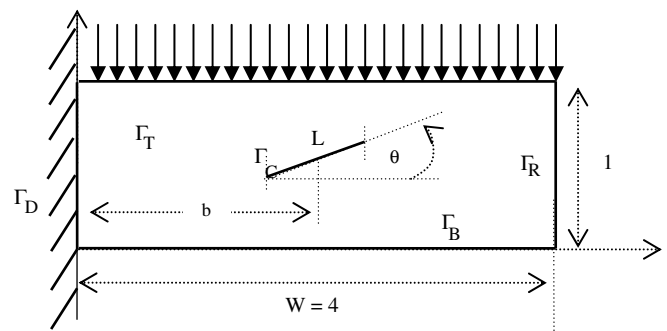


Fig. 3. A cantilever beam with a crack.

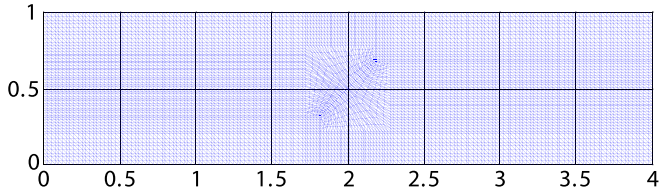


Fig. 4. Triangular mesh of finite element on the reference domain with the crack in the middle.

racy is set to $\epsilon_{tol} = 10^{-4}$. The greedy algorithm found $N_{max} = 34$. It means that 34 sampling points in the parameter space are needed to create the desired RBM model. The distribution of sample set P_N is shown in Fig. 5.

To examine the asymptotic error estimation, a parameter set S_{test} with sample size of $n_{test} = 500$ is randomly selected over the parameter domain \mathcal{D} : the averaged output errors $\Delta_{N,M,avg}^s$ and $\Delta_{N,exact,avg}^s$ are evaluated over entire S_{test} . The comparison of the averaged output errors as a function of N is plotted in Fig. 6. The comparison between the asymptotic output error $\Delta_{N,M}^s(\mu)$ and exact output error $\Delta_{N,exact}^s(\mu)$ for the two parameters of $\mu = (2.3936, 0.3681, 43.3353^\circ)$ and $\mu = (1.6988, 0.6707, 33.8238^\circ)$ are also plotted in Figs. 7 and 8, respectively. These results indicate that the asymptotic error estimation is reliable, and for $N \geq 3$, the asymptotic error estimation is in good agreements with the exact error. Therefore, it is very effective. The results also suggest a very fast convergence rate of RBM for an $N \ll \aleph$. To examine our asymptotic error more precisely, the maximum error difference of $|\Delta_{N,M}^s(\mu_{max}) - \Delta_{N,exact}^s(\mu_{max})|$ and the effectivity $\eta = \Delta_{N,M}^s(\mu_{max}) / \Delta_{N,exact}^s(\mu_{max})$ over the entire parameter set $S_{test} \in D$ are also provided at the greedy step of $N_{max} = 34$. We found that $|\Delta_{N,M}^s(\mu_{max}) - \Delta_{N,exact}^s(\mu_{max})|$ is 3.1570×10^{-7} and $\eta = 0.9957 \approx 1$ which show that the asymptotic error estimation is very effective and accurate.

7.2.2. Output bound condition and monotonic convergence property

The output bound condition which is one of the main concerns of this work is investigated here. Three FEM meshes of dimension $\aleph_{ref} = 30,760$, $\aleph \equiv \aleph_{D_2} = 17,344$ for division D_2 and $\aleph_{D_1} = 4,392$ for

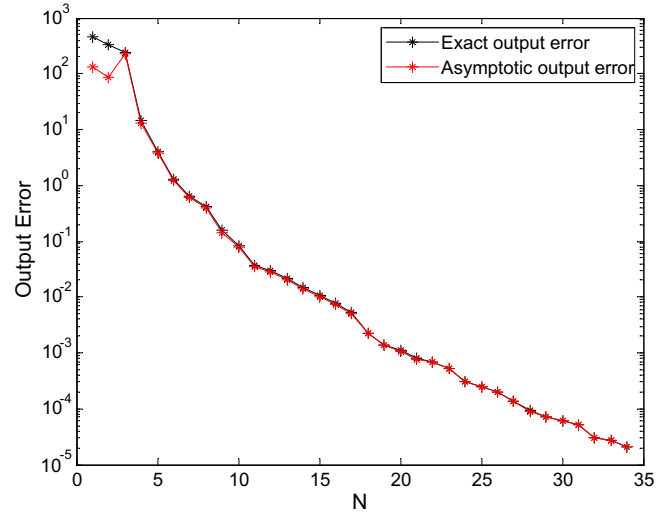


Fig. 6. Comparison between the averaged asymptotic error and averaged exact error.

division D_1 are used. The FEM is first used to obtain a reference output using the very large dimension \aleph_{ref} , which is nearly twice as large as \aleph_{D_2} and seventh times as large as \aleph_{D_1} in the FEM approximation space \mathbb{S} . The output of the GP_RBM and SGP_RBM for domain divisions D_i denoted as $(\bar{s}_N(\mu))_{D_i}$ and $(\bar{s}_N(\mu))_{D_i}$, where $i = 1, 2$, are evaluated.

For three randomly selected parameters from $S_{test} \subset \mathcal{D}$, $\mu_{test-1} = (2.4883, 0.5086, 47.6885^\circ)$, $\mu_{test-2} = (2.4943, 0.5741, 20.8077^\circ)$, and $\mu_{test-3} = (1.5589, 0.6695, 42.7393^\circ)$, compliance outputs of the GP_RBM, the reference FEM, and the SGP_RBM are compared as shown in Table 2 and Fig. 9. The results show clearly output-bound properties as well as monotonic convergence property for the two meshes D_1 and D_2 , which confirms our theory. For effective discussion on monotonic convergence property, Table 3 shows the bound gaps of $G_{D_i}(\mu)$, $i = 1, 2$, to assert that $G_{D_1}(\mu) \geq G_{D_2}(\mu)$ which confirms again our theory. These properties are very important in practical engineering application. Moreover,

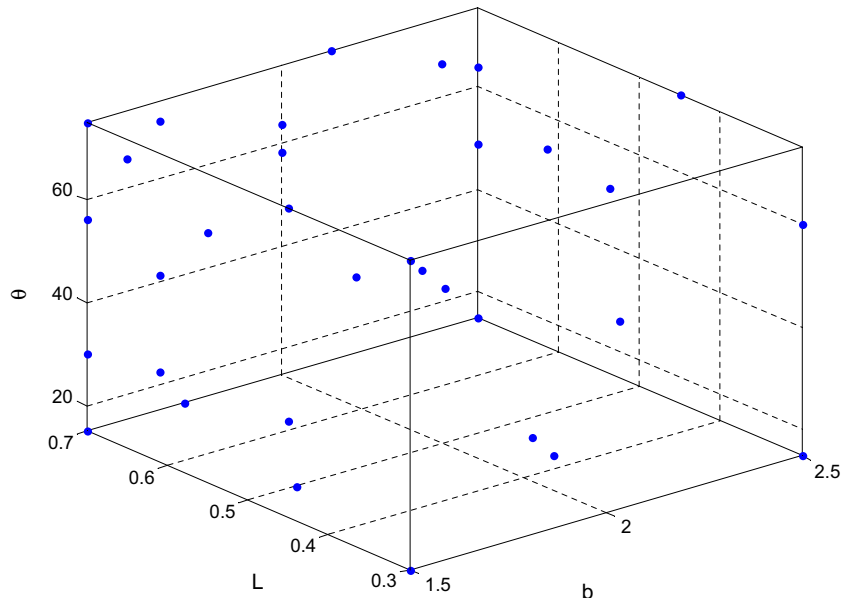


Fig. 5. Distribution of reduced-basis sample set P_N obtained by adaptive sampling procedure using the greedy algorithm ($N_{max} = 34$).

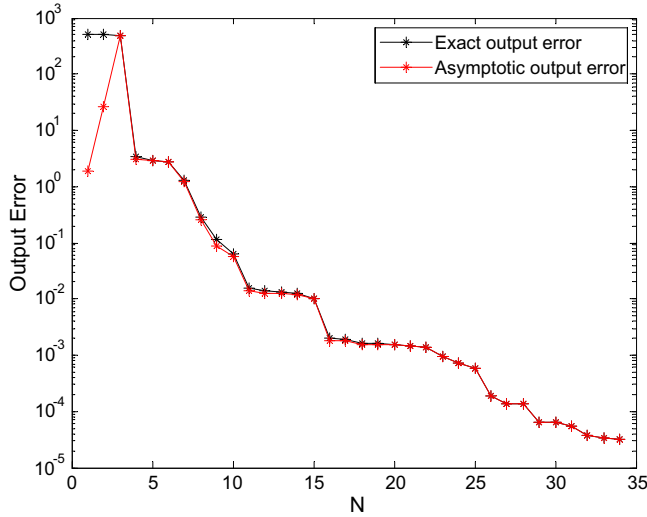


Fig. 7. Comparison between the asymptotic error and the exact output error for $\mu = (2.3936, 0.3681, 43.3353^\circ)$.

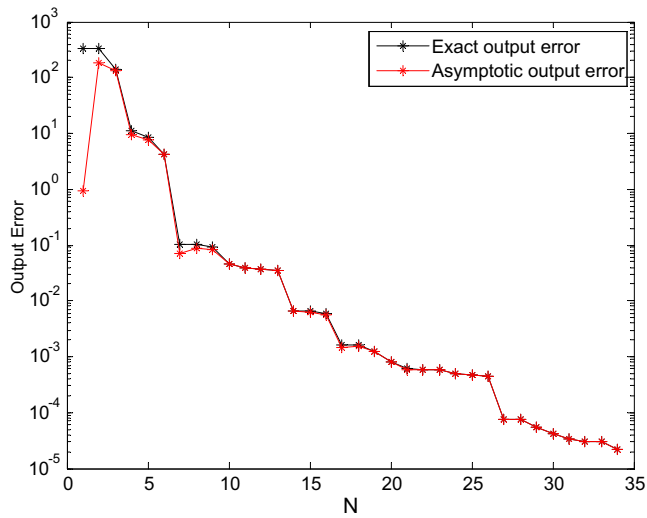


Fig. 8. Comparison between the asymptotic error and the exact output error for $\mu = (1.6988, 0.6707, 33.8238^\circ)$.

Table 3 confirms that a tighter bound can be obtainable using a finer mesh.

Note that the approach of producing the error bounds in the present approach of using both GP_RBM and SGP_RBM is different from the standard RBM approach. We do not evaluate the RBA-error anymore for the purpose of producing the error bounds for the RBM outputs. The meaning of the output bounds and the bound gaps are also different. The present RBM approach provides bounds with respect to the exact outputs, while the standard RBM is with respect to the fine FEM model.

7.2.3. Computational savings

The online computation cost for $\tilde{s}_N(\mu)$ and $\bar{s}_N(\mu)$ is then compared with that of the FEM output $\bar{s}(\mu)$. Based on the same discretization D_2 of dimension $N_{D_2} = 17,344$, the CPU time for evaluation of $\tilde{s}_N(\mu)$, $\bar{s}_N(\mu)$ and the FEM output evaluation of $\bar{s}(\mu)$ are listed in Table 4. We found that the CPU time for the output evaluation using the FEM is much longer than that of using both the proposed GP_RBM and SGP_RBM.

Table 2

Compliance outputs by GP_RBM, reference FEM, and SGP_RBM for the coarse mesh D_1 and for the fine mesh D_2

| $\mu \equiv (b, L, \theta)$ | Compliance output: $s(\mu)$ | | | | |
|-----------------------------|-----------------------------|--------------------------|--|--------------------------|--------------------------|
| | Lower bound | | Reference FEM output ($N = 30,760$) | Upper bound | |
| | $(\bar{s}_N(\mu))_{D_1}$ | $(\bar{s}_N(\mu))_{D_2}$ | | $(\bar{s}_N(\mu))_{D_2}$ | $(\bar{s}_N(\mu))_{D_1}$ |
| $\mu_{\text{test-1}}$ | 676.3851 | 681.0425 | 681.7525 | 683.4469 | 684.8074 |
| $\mu_{\text{test-2}}$ | 675.4433 | 680.7937 | 681.7268 | 684.0950 | 685.8932 |
| $\mu_{\text{test-3}}$ | 684.5895 | 688.8946 | 689.7194 | 691.5191 | 693.0566 |

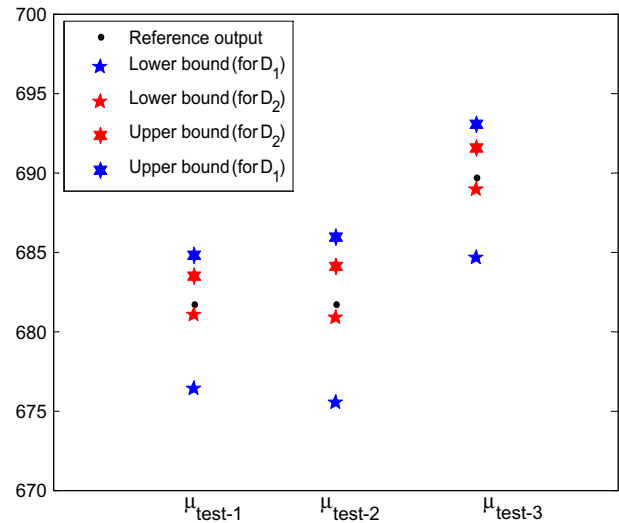


Fig. 9. Illustration of the reference FEM output vs the GP_RBM, and SGP_RBM outputs for three selected parameter points (D_2 : fine mesh, D_1 : coarse mesh).

Table 3

Bound gaps for the two different background meshes, D_1 and D_2

| $\mu \equiv (b, L, \theta)$ | Bound difference: $G_{D_i} = (\bar{s}_N(\mu))_{D_i} - (\tilde{s}_N(\mu))_{D_i}, i = 1, 2$ | |
|-----------------------------|---|-------------------|
| | D_1 (coarse mesh) | D_2 (fine mesh) |
| $\mu_{\text{test-1}}$ | 8.4223 | 2.4044 |
| $\mu_{\text{test-2}}$ | 10.4499 | 3.3013 |
| $\mu_{\text{test-3}}$ | 8.4671 | 2.6245 |

Table 4

Comparison of RBM online computational time and FEM computational time

| N | Online evaluation time for outputs, $s(\mu)$ (s) | | |
|---|--|-----------------------|------------------------|
| | GP_RBM | SGP_RBM | Total online time |
| 20 | 0.56×10^{-3} | 0.54×10^{-3} | 1.1×10^{-3} |
| 30 | 0.64×10^{-3} | 0.64×10^{-3} | 1.28×10^{-3} |
| 34 | 0.67×10^{-3} | 0.66×10^{-3} | 1.33×10^{-3} |
| FEM evaluation time for $\bar{s}(\mu)$ ($N = 17,344$) (s) | | | 0.9289 \approx 1 (s) |

To precisely quantify the saving, we define the CPU time-saving factor α as

$$\alpha = \frac{t_{\text{FEM}}}{t_{\text{GP_RBM}} + t_{\text{SGP_RBM}}}, \tag{73}$$

where t_{FEM} is CPU time for output evaluation using the FEM, $t_{\text{GP_RBM}}$ and $t_{\text{SGP_RBM}}$ are CPU time for “online” output evaluations using GP_RBM and SGP_RBM. Table 5 shows the CPU time-saving factor

Table 5

Time-saving by using RBM including GP_RBM and SGP_RBM compared to FEM for $N = 34$

| Computation time | | | α |
|----------------------------------|-----------------------|----------------------------------|----------------------|
| t_{GP_RBM} (s) | t_{SGP_RBM} (s) | $t_{GP_RBM} + t_{SGP_RBM}$ (s) | |
| 0.67×10^{-3} | 0.66×10^{-3} | 1.33×10^{-3} | $698.42 \approx 700$ |
| $t_{FEM} = 0.9289 \approx 1$ (s) | | | |

for the cantilever beam problem. The computational saving factor α is nearly as large as 700.

8. Conclusion

A new fast computational method called smoothed Galerkin projection reduced-basis method (SGP_RBM) is developed for real-time computation of upper bounds of the outputs of linear elastic solid mechanics problems in this work. The smoothed bilinear form is employed in the well-known reduced-basis method to establish the theoretical framework of the SGP_RBM. The important properties of the proposed method have been proven theoretically and investigated numerically on a sample problem. Both the theoretical analysis and numerical results have demonstrated that the proposed SGP_RBM has the following features:

- (i) The method has the same fast convergence rate of the standard reduced-basis method.
- (ii) We presented for the first time a numerical method to obtain, in real-time, both the *exact* upper and lower bounds: the SGP_RBM gives an upper bound and the GP_RBM gives a lower bound.
- (iii) The conventional expensive reduced-basis error estimations are not required for the upper bound output.
- (iv) A less precise but more efficient asymptotic error estimation can be employed only for the construction of the reduced-basis sample set.
- (v) In the present approach, we do not require “very fine” mesh for building the SGP_RBM and GP_RBM models. The mesh density can be determined by the desired accuracy for the outputs. This is because our output bounds are always with respect to the *exact* outputs regardless of the mesh density of the model. This means that even the offline computational cost can be saved significantly.
- (vi) The present approach is very efficient computationally. For the example problem, the present RBM approach is 700 times faster than the finite element approach. Even better computational efficiency can be expected for large-scale systems.

References

- [1] G.R. Liu, S.S. Quek, *Finite Element Method: A Practical Course*, Butterworth-Heinemann, Burlington, MA, 2003.
- [2] Eduardo R De Arantes E. Oliveira, Theoretical foundations of the finite element method, *Int. J. Solids Struct.* 4 (1968) 929–952.
- [3] K.J. Bathe, *Finite Element Procedures*, Prentice Hall, Upper Saddle River, NJ, 1996.
- [4] J.N. Reddy, *An Introduction to the Finite Element Method*, second ed., McGraw-Hill, NY, 2003.
- [5] O.C. Zienkiewicz, R.L. Taylor, *The Finite Element Method*, fifth ed., Butterworth-Heinemann, Oxford, UK, 2000.
- [6] D. Braess, *Finite Elements: Theory, Fast Solvers and Applications in Solid Mechanics*, second ed., Cambridge University Press, Cambridge, 2001.
- [7] P. Boresi, Ken P. Chong, Sunil Saigal, *Approximate Solution Methods in Engineering Mechanics*, second ed., John Wiley & Sons Inc., NJ, 2003.
- [8] G.R. Liu, M.B. Liu, *Smoothed Particle Hydrodynamics-A Meshfree Particle Method*, World Scientific, Singapore, 2003.
- [9] G.R. Liu, *Meshfree Methods: Moving Beyond the Finite Element Method*, CRC Press, Boca Raton, USA, 2002.
- [10] G.R. Liu, Y.T. Gu, A Point Interpolation Method for Two-dimensional Solids, *Int. J. Numer. Methods Engrg.* 50 (2001) 937–951.
- [11] G.R. Liu, Khin Zaw, Y.Y. Wang, Rapid inverse parameter estimation using reduced-basis approximation with asymptotic error estimation, *Comput. Methods Appl. Mech. Engrg.* (2008), doi:10.1016/j.cma.2008.03.012.
- [12] C. Prud'homme, D.V. Rovas, K. Veroy, L. Machiels, Y. Maday, A.T. Patera, G. Turinici, Reliable real-time solution of parametrized partial differential equations: Reduced-basis output bound methods, *J. Fluids Engrg.* 124 (2002) 70–80.
- [13] K. Veroy, *Reduced-Basis Methods Applied to Problems in Elasticity Analysis and Application*, Ph.D. thesis, Massachusetts Institute of Technology, 2003.
- [14] N.C. Nguyen, *Reduced-basis Approximation and a Posteriori Error Bounds for Nonaffine and Nonlinear Partial Differential Equations: Application to Inverse Analysis*, Ph.D. thesis, MIT Alliance, Singapore, 2005.
- [15] K. Veroy, A.T. Patera, Certified real-time solution of the parameterized steady incompressible Navier–Stokes equations: rigorous reduced-basis a posteriori error bounds, *Int. J. Numer. Methods Fluids* 47 (2005) 773–788.
- [16] S. Sen, K. Veroy, D.B.P. Huynh, S. Deparis, N.C. Nguyen, A.T. Patera, “Natural Norm” a posteriori error estimators for reduced-basis approximation, *J. Comput. Phys.* 217 (2006) 37–62.
- [17] G. Rozza, K. Veroy, On the stability of the reduced basis method for Stokes equations in parameterized domains, *Comput. Methods Appl. Mech. Engrg.* 196 (2007) 1244–1260.
- [18] A.T. Patera, E.M. Rønquist, Reduced basis approximation and a posteriori error estimation for a Boltzmann model, *Comput. Methods Appl. Mech. Engrg.* 196 (2007) 2925–2942.
- [19] D.B.P. Huynh, A.T. Patera, Reduced-basis approximation and a posteriori error estimation for stress intensity factor, *Int. J. Numer. Meth. Engrg.* 00 (2006) 1–6.
- [20] G.R. Liu, G.Y. Zhang, K.Y. Dai, Y.Y. Wang, Z.H. Zhong, G.Y. Li, X. Han, A linearly conforming point interpolation method (LC-PIM) for 2D mechanics problems, *Int. J. Comput. Methods* 2 (2005) 645–665.
- [21] G.Y. Zhang, G.R. Liu, Y.Y. Wang, H.T. Huang, Z.H. Zhong, G.Y. Li, X. Han, A linearly conforming point interpolation method (LC-PIM) for three-dimensional elasticity problems, *Int. J. Numer. Methods Engrg.* 72 (2007) 1524–1543.
- [22] G.R. Liu, G.Y. Zhang, Upper bound solution to elasticity problems: a unique property of the linearly conforming point interpolation method (LC-PIM), *Int. J. Numer. Mech. Engrg.* (2007), doi:10.1002/nme.2204.
- [23] J.S. Chen, C.T. Wu, S. Yoon, Y. You, A stabilized conforming nodal integration for Galerkin mesh-free methods, *Int. J. Numer. Methods Engrg.* 50 (2001) 435–466.
- [24] T.J.R. Hughes, *The Finite Element Method*, Prentice-Hall, London, 1987.
- [25] G.R. Liu, A generalized gradient smoothing technique and the smoothed bilinear form for Galerkin formulation of a wide class of computational methods, *Int. J. Comput. Methods* 5 (2) (2008) 199–236.
- [26] G.R. Liu, K.Y. Dai, T.T. Nguyen, A smoothed finite element method for mechanics problems, *Comput. Mech.* 39 (2007) 859–877.
- [27] G.R. Liu, T.T. Nguyen, K.Y. Dai, K.Y. Lam, Theoretical aspects of the smoothed finite element method (SFEM), *Int. J. Numer. Methods Engrg.* 71 (2007) 902–930.
- [28] G.Y. Zhang, G.R. Liu, T.T. Nguyen, C.X. Song, X. Han, Z.H. Zhong, G.Y. Li, The upper bound property for solid mechanics of the linearly conforming radial point interpolation method (LC-RPIM), *Int. J. Comput. Methods* 4 (2007) 521–541.
- [29] G.R. Liu, T.T. Nguyen, K.Y. Lam, An edge-based smoothed finite element method (E-SFEM) for free and forced vibration analysis, *J. Sound Vib.* (2008) (revised).
- [30] G.R. Liu, A weakened weak (W2) form for a unified formulation of compatible and incompatible displacement method, *Int. J. Numer. Methods Engrg.*, submitted for publication.